

Observation of multi-component atomic Schrödinger cat states of up to 20 qubits

Chao Song^{1,*}, Kai Xu^{2,4,*}, Hekang Li^{2,*}, Yuran Zhang^{2,5}, Xu Zhang¹, Wuxin Liu¹,
Qiujiang Guo¹, Zhen Wang¹, Wenhui Ren¹, Jie Hao³, Hui Feng³, Heng Fan^{2,4,†}

Dongning Zheng^{2,4,‡}, Dawei Wang^{1,4}, H. Wang^{1,6,§} and Shiyao Zhu^{1,6}
¹ Interdisciplinary Center for Quantum Information and

Zhejiang Province Key Laboratory of Quantum Technology and Device,
Department of Physics, Zhejiang University, Hangzhou 310027, China,

² Institute of Physics, Chinese Academy of Sciences, Beijing 100190, China,

³ Institute of Automation, Chinese Academy of Sciences, Beijing 100190, China,

⁴ CAS Center for Excellence in Topological Quantum Computation,
University of Chinese Academy of Sciences, Beijing 100190, China,

⁵ Beijing Computational Science Research Center, Beijing 100094, China,

⁶ Synergetic Innovation Center of Quantum Information and Quantum Physics,
University of Science and Technology of China, Hefei, Anhui 230026, China

(Dated: January 2, 2022)

We report on deterministic generation of 18-qubit *genuinely entangled* Greenberger-Horne-Zeilinger (GHZ) state and multi-component atomic Schrödinger cat states of up to 20 qubits on a quantum processor, which features 20 superconducting qubits interconnected by a bus resonator. By engineering a one-axis twisting Hamiltonian enabled by the resonator-mediated interactions, the system of qubits initialized coherently evolves to an over-squeezed, non-Gaussian regime, where atomic Schrödinger cat states, i.e., superpositions of atomic coherent states including GHZ state, appear at specific time intervals in excellent agreement with theory. With high controllability, we are able to take snapshots of the dynamics by plotting quasidistribution Q -functions of the 20-qubit atomic cat states, and globally characterize the 18-qubit GHZ state which yields a fidelity of 0.525 ± 0.005 confirming *genuine eighteen-partite entanglement*. Our results demonstrate the largest entanglement controllably created so far in solid state architectures, and the process of generating and detecting multipartite entanglement may promise applications in practical quantum metrology, quantum information processing and quantum computation.

The capability of controllably entangling multiple particles is central to fundamental test of quantum theory [1], and represents a key prerequisite for quantum information processing. There exist various kinds of multipartite entangled states, among which the Greenberger-Horne-Zeilinger (GHZ) states, i.e., the 2-component atomic Schrödinger cat states, are particularly appealing and useful [2]. These states play a key role in quantum-based technologies, including open-destination quantum teleportation [3], concatenated error correcting codes [4], quantum simulation [5], and high-precision spectroscopy measurement [6]. In principle, the number of particles that can be deterministically entangled in a quantum processor is a benchmark of its capability in processing quantum information. However, it is difficult to scale up this number since the conventional step-by-step gate methods require long control sequences which increase exposure to perturbing noise. A shortcut is to realize the free evolution under a nonlinear Hamiltonian with, e.g., one-axis twisting, and the system of qubits initialized in an atomic coherent state is predicted to evolve to squeezed spin states [7], and then to the multi-component atomic Schrödinger cat states [8], i.e., superpositions of atomic coherent states including GHZ state [9].

Engineering fully controllable and highly coherent multipartite quantum computing platforms remains an outstanding challenge. Several physical platforms are being

explored [10–15], and a series of experiments for generating multipartite entanglement were reported [14–23]. Some of these experiments involve local detections of only the subsystems [15, 19]. Multipartite entanglement, in particular the GHZ state which possesses global entanglement, would be better characterized by synchronized detections of all system parties and was achieved with 14 trapped ions [20], 12 photons [21], 18 photonic qubits exploiting 6 photons [22], and 12 superconducting qubits [23]. In particular, previously we reported the production and full tomography of the 10-qubit GHZ state and the implementation of high-fidelity two-qubit gate with an all-to-all connected superconducting quantum processor [14, 24], where each qubit can be individually controlled and qubit-qubit interactions can be turned on and off as desired.

In this letter we introduce our latest upgrade, a more powerful 20-qubit superconducting quantum processor featuring all-to-all connectivity with programmable qubit-qubit couplings mediated by a bus resonator. With all qubits designed to be uniformly coupled to the bus resonator, we engineer a one-axis twisting Hamiltonian by identically detuning the qubits from the bus resonator. Free evolution under the engineered Hamiltonian steers the system to squeezed spin states, and then to over-squeezed regime with suppositions of atomic coherent states at specific time intervals, which are experimen-

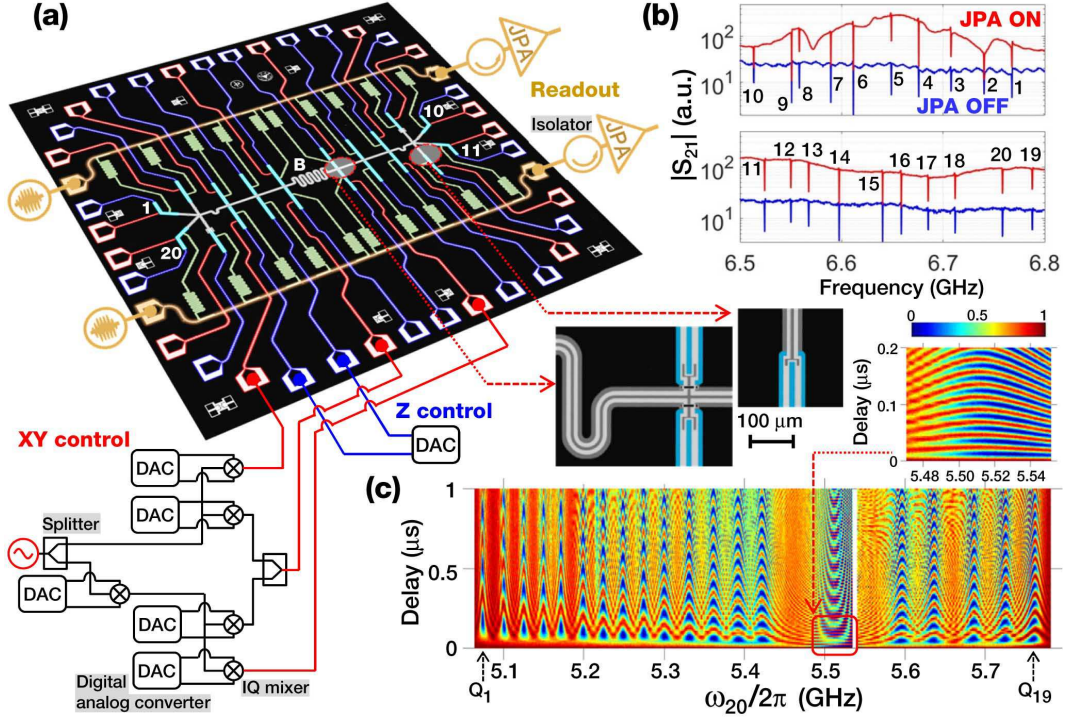


FIG. 1. (a) False-color circuit image showing 20 superconducting qubits (line shapes in cyan that are labeled clockwise from 1 to 20) interconnected by a central bus resonator B (grey). Each qubit has its own flux bias line (blue) for Z control, and 16 qubits have individual microwave lines (red) for XY control, while Q_4 , Q_7 , Q_{14} , and Q_{17} share the microwave lines of neighboring qubits. Each qubit has its own readout resonator (green), which couples to one of the two transmission lines (orange) for simultaneous readout. Also shown are zoomed-in views of representative qubit-bus resonator coupling capacitors with different capacitance values at spots as indicated, and illustrative schematics of the measurement setup showing wirings to the circuit chip, where we cascade two stages of sideband mixings to generate microwave pulses that cover tones with a 1 GHz-bandwidth while maintaining the capability of tracking the relative phases among tones. (b) Signal spectra through the transmission lines $|S_{21}|$ while all qubits are in $|0\rangle$. Shown are the amplitudes of the demodulated signals as functions of signal frequency when the JPAs are “ON” (red) and “OFF” (blue). The qubits’ readout resonators, labeled from 1 to 20, are visible as dips on the spectra. (c) Swap spectroscopy of Q_{20} , which is obtained by exciting Q_{20} to $|1\rangle$ and then measuring its $|1\rangle$ -state probability as function of both the qubit frequency and delay time. The probability data, corrected for elimination of the measurement errors [27], are from two continuous scans separated by the vertical white stripe. During the scans the other 19 qubits are sorted in frequency with Z controls and are identified by the well-resolved Chevron patterns, which are due to coherent energy exchanges between Q_{20} and the qubits mediated by the bus resonator B . Zoomed-in view is the direct energy exchange between Q_{20} and B .

tally captured. The final GHZ states are characterized by synchronized local manipulations and detections of all qubits, and we measure a fidelity figure of 0.525 ± 0.005 for 18 qubits, which confirms the genuine eighteen-partite entanglement [25].

The new version of the superconducting quantum processor and critical peripheral electronics are illustrated in Fig. 1(a), which consists of 20 frequency-tunable transmon qubits, labeled as Q_j for $j = 1$ to 20, surrounding a central coplanar waveguide bus resonator (B), whose resonant frequency is fixed at $\omega_B/2\pi \approx 5.51$ GHz. Qubit-resonator (Q_j - B) coupling strengths g_j are designed to be uniform, and measured $g_j/2\pi$ values range from 24.1 to 30.1 MHz. Qubits are detected through their respective readout resonators, whose signal spectra are shown in Fig. 1(b). We use impedance matched Josephson para-

metric amplifiers (JPAs) and an optimized arrangement of the qubit frequencies, ω_j^m , during the readout to enhance the signal-to-noise ratio.

All qubits are individually tunable with high flexibility, and we show an example in Fig. 1(c) by measuring Q_{20} ’s swap spectroscopy while we equally space the other 19 qubits in frequency around the resonator B . Typical qubit energy relaxation times, T_1 , are in the range of 20 to 50 μ s. With a proper arrangement of the qubit idle frequencies, ω_j , where qubit initializations and single-qubit rotations are applied, fidelity values of the simultaneous single-qubit $\pi/2$ rotational gates used in the GHZ experiment are all above 0.99 as estimated by quantum state tomography and simultaneous randomized benchmarking. See Supplemental Material for more details on the device and its operations [26].

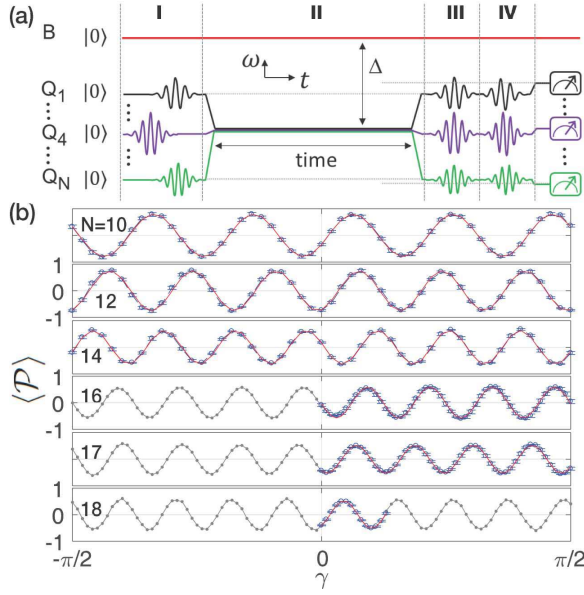


FIG. 2. (a) Pulse sequence for generating and characterizing the N -qubit GHZ state. For a qubit who shares its neighbor's microwave line, e.g., Q_4 which shares Q_5 's, its first $X_{\pi/2}$ rotational pulse (sinusoids in zone I), which has an amplitude almost ten times larger than Q_5 's own rotational pulse and therefore may dispersively drive Q_5 as well, starts earlier while Q_5 is in $|0\rangle$ in order to reduce the extra phase picked up by Q_5 due to this dispersive drive. (b) N -qubit GHZ parity oscillations. For each data point (blue circles), we repeat the state preparation and measurement sequence about 30×2^N times to find the raw 2^N occupational probabilities and then apply readout corrections to eliminate the measurement errors [27], following which we use maximum likelihood estimation to validate the occupational probabilities and calculate the parity value $\langle P \rangle$. To estimate error bars, we divide the complete dataset into subgroups, each containing about 5×2^N samplings, and the error bars correspond to the standard deviations of those calculated from these subgroups. Red lines are sinusoid fits, with the fringe amplitudes corresponding $\rho_{00\dots 0, 11\dots 1}$. For $N = 16$ to 18 , repeated measurements with the sampling size of about 30×2^N times over a full range of $\gamma \in [-\pi/2, \pi/2]$ take too long. Therefore we reduce the range of γ that has enough samplings. As such grey dots connected by dashed lines are calculated from the experimental data with reduced sampling size, which are plotted only for visual guide of the oscillations.

With each of the 20 qubits being addressable, the system Hamiltonian is

$$H_1/\hbar = \omega_B a^\dagger a + \sum_{j=1}^{20} [\omega_j(t)|1_j\rangle\langle 1_j| + g_j(\sigma_j^+ a + \sigma_j^- a^\dagger)] + \sum_{j=1}^{20} \lambda_{j,j+1}^c (\sigma_j^+ \sigma_{j+1}^- + \sigma_j^- \sigma_{j+1}^+), \quad (1)$$

where $\omega_j(t)$ ($\gg g_j$) is tunable within a time scale of a few nanoseconds, σ_j^+ (σ_j^-) is the raising (lowering) operator of Q_j , a^\dagger (a) is the creation (annihilation) operator of

B , and $\lambda_{j,j+1}^c$ describes the crosstalk couplings between neighboring qubits (Subscripts in $\lambda_{j,j+1}^c$ run cyclically from 1 to 20). Although more qubits are integrated in this processor, the measured $\lambda_{j,j+1}^c/2\pi$ values are seen to be reduced from ~ 2 MHz in the previous 10-qubit version [14, 28] to around 1 MHz or less since we separate the qubits physically as much as possible (see Fig. 1(a)). Note that there may exist those qubit-qubit crosstalk couplings beyond neighboring pairs, which should be relatively small and are not included in Eq. (1).

As demonstrated previously [14], the unique feature of this architecture is that, although qubits are physically separated by the bus resonator B , the qubit-qubit coupling mediated by B can be programmed with fast Z controls to match or detune their frequencies [14, 24]. More remarkably, in our processor, we can selectively entangle N of the 20 qubits by detuning the selected qubits from the resonator by the same amount Δ ($\gg g_j$), with the other qubits being far off-resonant. When resonator B is initially in vacuum, the effective Hamiltonian for these N qubits, relabeled by Q_j with j going from 1 to N , in the frame rotating at the detuned qubit frequency is [8, 9]

$$H_2/\hbar = \sum_{\{j,k\} \in N} \frac{g_j g_k}{\Delta} (\sigma_j^+ \sigma_k^- + \sigma_j^- \sigma_k^+) + \sum_{j=1}^N \frac{g_j^2}{\Delta} |1_j\rangle\langle 1_j| + \sum_{j=1}^N \lambda_{j,j+1}^c (\sigma_j^+ \sigma_{j+1}^- + \sigma_j^- \sigma_{j+1}^+), \quad (2)$$

where $\{j,k\}$ takes all possible pairs within the N qubits and subscripts in $\lambda_{j,j+1}^c$ run cyclically from 1 to N .

The scenario of a system of N identical two-level atoms interacting collectively and dispersively with a single mode electromagnetic field in a cavity has been theoretically investigated [8, 9]. In our experiment we position the qubits 330 MHz below $\omega_B/2\pi$ for all the effective qubit-qubit couplings (190 terms) in the first summation of Eq. (2), $|g_j g_k/2\pi\Delta|$, to be ~ 2 MHz while the few (< 20 terms) neighboring couplings $\lambda_{j,j+1}^c/2\pi$ are from 0.5 to 1 MHz. Therefore we can ignore $\lambda_{j,j+1}^c$ and those relatively small qubit-qubit crosstalk couplings beyond neighboring pairs (not included in Eq. (1)) for now and assume that couplings within all qubit pairs are approximately equal, so that the theory predictions [8, 9] can be adapted to our experiment. We emphasize that the imperfection in uniformity has been taken into account by numerical simulations using device parameters based on the Hamiltonian in Eq. (1), and we find decent agreement between our experimental results and the simplified theoretical treatment in Refs. [8, 9].

With uniform couplings noted as $\lambda = \overline{g_j g_k}/\Delta$, we now apply the spin representation of qubit states and define the collective spin operators $\mathcal{S}^+ = \sum_j \sigma_j^+$, $\mathcal{S}^- = \sum_j \sigma_j^-$, and $\mathcal{S}_z = \sum_j \sigma_{z,j}$. The term $\sum \lambda (\sigma_j^+ \sigma_k^- + \sigma_j^- \sigma_k^+)$ in

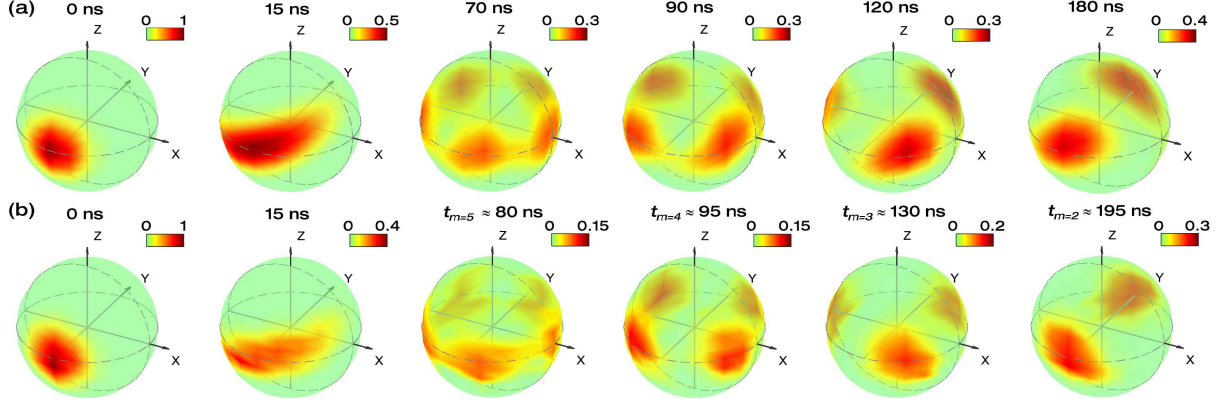


FIG. 3. Dynamics of the 20-qubit system illustrated with the quasidistribution Q -function. (a) Numerical simulations of $Q(\theta, \phi)$ in the spherical polar plots at specific time intervals predicted by Eq. (1) ignoring decoherence, after the qubits are initialized in an atomic coherent state $|\pi/2, -\pi/2\rangle$. (b) Experimental measured $Q_{\text{exp}}(\theta, \phi)$ at time intervals as listed. Additional single-qubit dynamical phases, which are accumulated during the qubit frequency tuning process and not included in the calculations in (a), are numerically added to rotate the plots in (a) for a better visual match with the $Q_{\text{exp}}(\theta, \phi)$ plots in (b). The difference in the time steps as listed between (a) and (b) may be due to various factors such as uncertainties in some device parameters including Δ and g_j , imperfection in the experimental pulse sequences, and, most likely, the existence of the small qubit-qubit crosstalk coupling terms beyond neighboring pairs that are not included in Eq. (1). Note that including all the small crosstalk coupling terms in the numerical simulation renders the Hamiltonian matrix less sparse and will considerably raise the computational complexity.

Eq. (2) is then transformed to $\lambda\mathcal{S}^+\mathcal{S}^- \rightarrow -\lambda\mathcal{S}_z^2$ ignoring trivial linear and constant terms, which is the one-axis twisting Hamiltonian. By initializing the N qubits identically so that each individual qubit points to the same direction represented by the angles (θ, ϕ) in its Bloch sphere, we write down the wavefunction of the atomic (spin) coherent state as

$$\psi(0) = |\theta, \phi\rangle = \left[\cos \frac{\theta}{2} |0\rangle + \sin \frac{\theta}{2} e^{i\phi} |1\rangle \right]^{\otimes N}. \quad (3)$$

Evolution of the wavefunction under the one-axis twisting Hamiltonian, $H = -\lambda\mathcal{S}_z^2$, was analytically obtained in Ref. [8], which shows that at particular time $t = \pi/m\lambda$, where m is an integer no less than 2, $\psi(0)$ evolves to a superposition of multiple atomic coherent states, i.e., it becomes an atomic Schrödinger cat state. In particular, at $m = 2$, it evolves to a superposition of two atomic coherent states, i.e., the N -qubit GHZ state,

$$\begin{aligned} \psi(t = \pi/2|\lambda|) &= e^{-iHt} |\theta, \phi\rangle = \frac{1}{\sqrt{2}} e^{-i(N-0.5)\pi/2} \\ &\times \left[\left| \theta, \phi - \frac{N-1}{2}\pi \right\rangle + e^{-i\pi/2} \left| \theta, \phi - \frac{N-3}{2}\pi \right\rangle \right]. \end{aligned} \quad (4)$$

Figure 2(a) shows the pulse sequence for generating and characterizing the N -qubit GHZ state. We start with initializing each of the N qubits in $(|0\rangle - i|1\rangle)/\sqrt{2}$, which collectively corresponds to an atomic coherent state $|\pi/2, -\pi/2\rangle$ in the (θ, ϕ) notation, by applying an $X_{\pi/2}$ rotational pulse at the qubit's idle frequency (sinusoids in zone I), following which we bias the N qubits

to $\Delta/2\pi \approx -330$ MHz for an optimized duration close to $\pi/2|\lambda|$ (zone II). The phase of each qubit's XY drive, which defines the rotational axis in the equator plane, is calibrated according to the rotating frame with respect to Δ , ensuring that all N qubits are in the same initial state just before their collective interactions are switched on [5, 14]. Right after the interactions we bias these qubits back to their respective idle frequencies, ω_j , for further operations if necessary, and then to their respective measurement frequencies, ω_j^m , for readout. We note that during the frequency tuning process qubits may gain different dynamical phases, i.e., the x - y axes rotate differently in the equator planes for different qubits, which can be determined by a separate phase tracking measurement followed by an optimization procedure (see Supplemental Material [26]).

The resulting GHZ state is a superposition of $|\pi/2, -N\pi/2\rangle$ and $|\pi/2, -(N-2)\pi/2\rangle$ in the collective spin representation, which can be transformed to a superposition of the N qubits all in $|0\rangle$ and those all in $|1\rangle$ by applying to each qubit a $\pi/2$ rotation around its x (N odd) or y (N even) axis. After such a transformation (sinusoids in zone III of Fig. 2(a)), the wavefunction is written as $(|00\dots 0\rangle + e^{i\varphi}|11\dots 1\rangle)/\sqrt{2}$, where $\varphi = \pi/2$ for uniform couplings. The diagonal elements of the GHZ density matrix $\rho_{00\dots 0}$ and $\rho_{11\dots 1}$ can be directly probed: For each state generation and characterization pulse sequence we simultaneously measure all qubits which returns an N -bit binary string, e.g., 01...0, showing the collapsed multiqubit state; we repeat the same pulse sequence multiple times and count the probabilities of find-

ing all N bits in 0 for $\rho_{00\dots0}$ and all those in 1 for $\rho_{11\dots1}$.

The off-diagonal elements $\rho_{00\dots0,11\dots1}$ and $\rho_{11\dots1,00\dots0}$ can be obtained by measuring the parity oscillations, defined as the expectation value of the operator $\mathcal{P}(\gamma) = \otimes_{j=1}^N (\cos \gamma Y_j + \sin \gamma X_j)$, which is given by $\langle \mathcal{P}(\gamma) \rangle = 2 |\rho_{00\dots0,11\dots1}| \cos(N\gamma + \varphi)$ for the abovementioned GHZ wavefunction [20]. Experimentally we apply to each qubit a rotation (sinusoids in zone IV of Fig. 2(a)) which bring the axis defined by the operator $\mathcal{P}(\gamma)$, i.e., the direction represented by the angles $(\pi/2, \pi/2 - \gamma)$ in each qubit's Bloch sphere, to the z axis, followed by simultaneous qubit readout. Repeating each state generation and measurement pulse sequence multiple times yields 2^N probabilities ($P_{00\dots0}, P_{00\dots1}, \dots, P_{11\dots1}$), and the parity is calculated as $\langle \mathcal{P} \rangle = P_{\text{even}} - P_{\text{odd}}$ with P_{even} (P_{odd}) corresponding to the summation of all those probabilities with even (odd) number of qubits in $|1\rangle$. The clear oscillation patterns of $\langle \mathcal{P}(\gamma) \rangle$, whose amplitude gives $|\rho_{00\dots0,11\dots1}|$, confirm the existence of coherence between the two states $|00\dots0\rangle$ and $|11\dots1\rangle$ (Fig. 2(b)). Using values of $\rho_{00\dots0}$, $\rho_{11\dots1}$, and $|\rho_{00\dots0,11\dots1}|$ obtained above, N -qubit GHZ state fidelities are calculated to be 0.817 ± 0.009 ($N = 10$), 0.775 ± 0.011 ($N = 12$), 0.655 ± 0.009 ($N = 14$), 0.579 ± 0.007 ($N = 16$), 0.549 ± 0.006 ($N = 17$), and 0.525 ± 0.005 ($N = 18$), all confirming genuine multipartite entanglement [25].

Furthermore, detailed dynamics connecting the atomic coherent state in Eq. (3) to the GHZ state in Eq. (4) under the one-axis twisting Hamiltonian was analytically given in Ref. [8], where squeezed spin states and more atomic Schrödinger cat states other than the final GHZ state sequentially appear. We are able to take snapshots of this dynamic process with up to 20 qubits by measuring the quasidistribution Q -function $Q(\theta, \phi) \propto \langle \theta, \phi | \rho(t) | \theta, \phi \rangle$, where $\rho(t)$ is the evolving multiqubit density matrix. For the 20 qubit case, we bias all qubits to $\Delta/2\pi \approx -470$ MHz since a newly added qubit, Q_{15} , is interfered by a two-level state defect at the previous entangling frequency. To obtain $Q(\theta, \phi)$, we rotate the axis defined by the angles (θ, ϕ) to the z axis for each qubit and do so simultaneously for all N qubits before joint readout: For $\theta < \pi/2$, we rotate by angle $-\theta$ around the $\phi - \pi/2$ axis in the equator plane and record $P_{00\dots0}$ as Q_{exp} ; for $\theta > \pi/2$, we rotate by angle $\pi - \theta$ around the $\phi + \pi/2$ axis in the equator plane to reduce the amplitude of the rotational pulse and record $P_{11\dots1}$ as Q_{exp} . Obtained values of Q_{exp} are plotted as functions of θ and ϕ in the spherical polar plots as shown in Fig. 3, together with the numerical simulations ignoring decoherence. We observe the squeezed spin regime at the beginning (~ 15 ns) and the atomic Schrödinger cat states which are superpositions of $m = 5, 4, 3$, and 2 atomic coherent states at $t_m \approx 80, 95, 130$, and 195 ns, respectively. It is seen that $t_m \propto 1/m$ as predicted in Ref. [8]. For an m -component atomic Schrödinger cat state of N qubits, the overlap between adjacent two components is

$\cos^N(\pi/m)$. Therefore to observe superpositions with more components one needs to increase N to reduce the overlap. We note that superpositions of up to 4 coherent states have been previously observed in cold atoms and superconducting cavities [29–31]. Here for the first time we observe the 5-component atomic Schrödinger cat state with $N = 20$ qubits.

In summary, our experiment demonstrates an upgraded and much more powerful version of the multiqubit-resonator-bus architecture for scalable quantum information processing, with 20 individually addressable qubits and programmable qubit-qubit couplings. Based on this device, we efficiently and deterministically generate the 18-qubit *genuinely entangled* GHZ state and multi-component atomic Schrödinger cat states of up to 20 qubits by engineering a one-axis twisting Hamiltonian. The high controllability and efficiency of our superconducting quantum processor demonstrate the great potential of an all-to-all connected circuit architecture for scalable quantum information processing.

Acknowledgments. This work was supported by the National Basic Research Program of China (Grants No. 2017YFA0304300 and No. 2016YFA0300600), the National Natural Science Foundations of China (Grants No. 11725419 and No. 11434008), and Strategic Priority Research Program of Chinese Academy of Sciences (Grant No. XDB28000000). Devices were made at the Nanofabrication Facilities at Institute of Physics in Beijing and National Center for Nanoscience and Technology in Beijing.

* C. S., K. X., and H.K. L. contributed equally to this work.

† hfan@iphy.ac.cn

‡ dzheng@iphy.ac.cn

§ hhwang@zju.edu.cn

- [1] W. H. Zurek, *Nature* **412**, 712 (2001).
- [2] D. M. Greenberger, M. A. Horne, A. Shimony, and A. Zeilinger, *Am. J. Phys.* **58**, 1131 (1990).
- [3] Z. Zhao *et al.*, *Nature* **430**, 54 (2004).
- [4] E. Knill, *Nature* **434**, 39 (2005).
- [5] C. Song *et al.*, *Phys. Rev. Lett.* **121**, 030502 (2018).
- [6] D. Leibfried *et al.*, *Science* **304**, 1476 (2004).
- [7] J. Ma, X. G. Wang, C. P. Sun, and F. Nori, *Phys. Rep.* **509**, 89 (2011).
- [8] G. S. Agarwal, R. R. Puri, and R. P. Singh, *Phys. Rev. A* **56**, 2249 (1997).
- [9] S. B. Zheng, *Phys. Rev. Lett.* **87**, 230404 (2001).
- [10] X-L. Wang *et al.*, *Phys. Rev. Lett.* **117**, 210502 (2016).
- [11] R. Barends *et al.*, *Nature* **534**, 222 (2016).
- [12] H. Bernien *et al.*, *Nature* **551**, 579 (2017).
- [13] D. Lu *et al.*, *npj Quantum Information* **3**, 45 (2017).
- [14] C. Song *et al.*, *Phys. Rev. Lett.* **119**, 180501 (2017).
- [15] N. Friis *et al.*, *Phys. Rev. X* **8**, 021012 (2018).
- [16] L. DiCarlo *et al.*, *Nature* **467**, 574 (2010).

- [17] M. Neeley *et al.*, Nature **467**, 570 (2010).
- [18] H. Paik *et al.*, Phys. Rev. Lett. **117**, 250502 (2016).
- [19] Y. H. Wang, Y. Li, Z. Q. Yin, and B. Zeng, npj Quantum Information **4**, 46 (2018).
- [20] T. Monz *et al.*, Phys. Rev. Lett. **106**, 130506 (2011).
- [21] H. S. Zhong *et al.*, Phys. Rev. Lett. **121**, 250505 (2018).
- [22] X. L. Wang *et al.*, Phys. Rev. Lett. **120**, 260502 (2018).
- [23] M. Gong *et al.*, Phys. Rev. Lett. **122**, 110501 (2019).
- [24] Q.J. Guo *et al.*, Phys. Rev. Lett. **121**, 130501 (2018).
- [25] O. Gühne and G. Tóth, Phys. Rep. **474**, 1 (2009).
- [26] See Supplemental Material for more information on the device and experiment.
- [27] Y. Zheng *et al.*, Phys. Rev. Lett. **118**, 210504 (2017).
- [28] K. Xu *et al.*, Phys. Rev. Lett. **120**, 050507 (2018).
- [29] M. Greiner, O. Mandel, T. W. Hnsch, and I. Bloch, Nature **419**, 51 (2002).
- [30] M. Hofheinz *et al.*, Nature **459**, 546 (2009).
- [31] B. Vlastakis *et al.*, Science **342**, 607 (2013).

Supplementary Material for “Observation of multi-component atomic Schrödinger cat states of up to 20 qubits”

Qubit-bus resonator coupling. Our sample is a superconducting circuit consisting of 20 Xmon qubits interconnected by a bus resonator, fabricated with three steps of aluminum depositions: Growth of the base wiring layer, double-angle evaporation of the junction bilayer, and coating the airbridge layer to connect signal lines and to short grounding pads. The overall design is similar to that reported in Ref. [14]. However, as illustrated in Fig. 1(a) of the main text, a key improvement in the current architecture is that the qubits, line shapes in cyan, are far separated as they go around the bus resonator in order to minimize the XX-type crosstalk couplings between neighboring qubits. Consequently, some of the qubits have to couple to the bus resonator B at spots away from both ends of the center trace of B via interdigitated capacitors. For the Q_j - B coupling strengths g_j to be relatively uniform, we choose different coupling capacitance values according to the coupling spots, as exemplified in Fig. 1(a) of the main text. Measured $g_j/2\pi$ values are listed in Tab. S1 and are in agreement with expectations.

Qubit manipulation. As shown in Fig. 1(a) of the main text, each qubit is frequency-tunable via its own flux bias line (Z control in blue) and can be coherently driven with its own or neighbor’s microwave line (XY control in red). The effective Z bias of each qubit due to a unitary bias applied to other qubits’ Z lines is calibrated, which yields the Z-crosstalk matrix \tilde{M}_Z as plotted in Fig. S1. The fact that only a few elements of \tilde{M}_Z , which describe the Z crosstalk magnitudes between certain neighboring pairs, reach maximum values at about 6.4%, indicates that the airbridges are connecting the grounding pads properly.

Taking into account the qubit’s weak anharmonicity, we carefully arrange the resonant frequencies of all qubits, ω_j , where qubits are initialized and operated with single-qubit rotational gates, to minimize any possible crosstalk errors, e.g., unwanted ZZ-type couplings. As such $\omega_j/2\pi$ values have to spread out as much as possible in a frequency span from 4.3 to 5.3 GHz (see ω_j in Tab. S1). To cover such a wide range of microwave tones while maintaining the capability of tracking the relative phases among tones, we cascade two stages of sideband mixings as illustrated in Fig. 1(a) of the main text. All together, our custom digital-to-analog converters, through the IQ mixing with a single-tone continuous microwave, can output phase-tracked microwave pulses with up to 20 tones targeting all 20 qubits for simultaneous XY rotational gates. Both quantum state tomography and simultaneous randomized benchmarking indicate that the gate fidelity values of the 40 ns-long $\pi/2$ rotations, used for the GHZ experiment, are above 0.99 (Fig. S2).

Qubit readout. As shown in Fig. 1(a) of the main text,

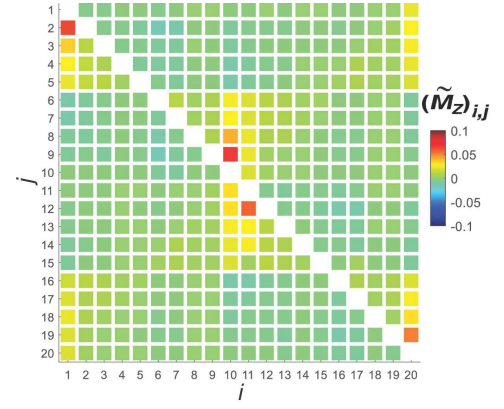


FIG. S1. **Z-crosstalk matrix** \tilde{M}_Z . Each element $(\tilde{M}_Z)_{i,j}$ represents the Z bias magnitude sensed by Q_j when Q_i is applied with a unitary Z bias.

each qubit, Q_j , dispersively interacts with its own readout resonator (green) that has a fixed tone at ω_j^r . All readout resonators couple to one of the two transmission lines (orange) across the circuit chip. At the output of each transmission line, an impedance matched Josephson parametric amplifier (JPA) is used to enhance the signal-to-noise ratio. To analyze the state of Q_j , we first quickly tune Q_j ’s frequency to ω_j^m via its Z control, and then pump its readout resonator to be populated with dozens of photons using microwave pulse through the corresponding transmission line. Since the qubit eigenstates $|0\rangle$ and $|1\rangle$ in the Pauli Z basis (along the z axis of the Bloch sphere) affect its readout resonator differently, we can observe the transmitted S_{21} signal near ω_j^r to tell the state of the qubit. Passing multi-tone signals targeting all ω_j^r through the transmission lines allows us to simultaneously read out N qubits by demodulating the S_{21} signals near their ω_j^r with custom analog-to-digital converters, which differentiates the 0 and 1 outcomes for each qubit and returns a joint outcome described by an N -bit binary string, e.g., 01...0, showing the collapsed state of N qubits. We run the same experimental sequence about 30×2^N times in order to obtain reliable raw probabilities, $\{P_{00\dots0}, P_{00\dots1}, \dots, P_{11\dots1}\}$, for 2^N basis states. Measurement in the X (Y) basis is achieved by inserting a Pauli Y (X) rotation on each qubit. The qubit $|0\rangle$ and $|1\rangle$ -state readout fidelity values, $F_{0,j}$ and $F_{1,j}$, are summarized in Tab. S1, which are used to correct the raw probabilities to eliminate the readout errors as done previously [27]. It is noted that for simultaneous readout, since qubits move down in frequency due to their readout resonators being populated with microwave photons, ω_j^m have to be carefully arranged to minimize any possible pairwise crosstalk influence (see ω_j^m in Tab. S1).

Phase tracking measurement. To perform the measurement of the quasidistribution Q -function, $Q(\theta, \phi)$, we need to identify the orientation of the x - y axes in the Bloch sphere for each qubit. In the experiment, as qubits

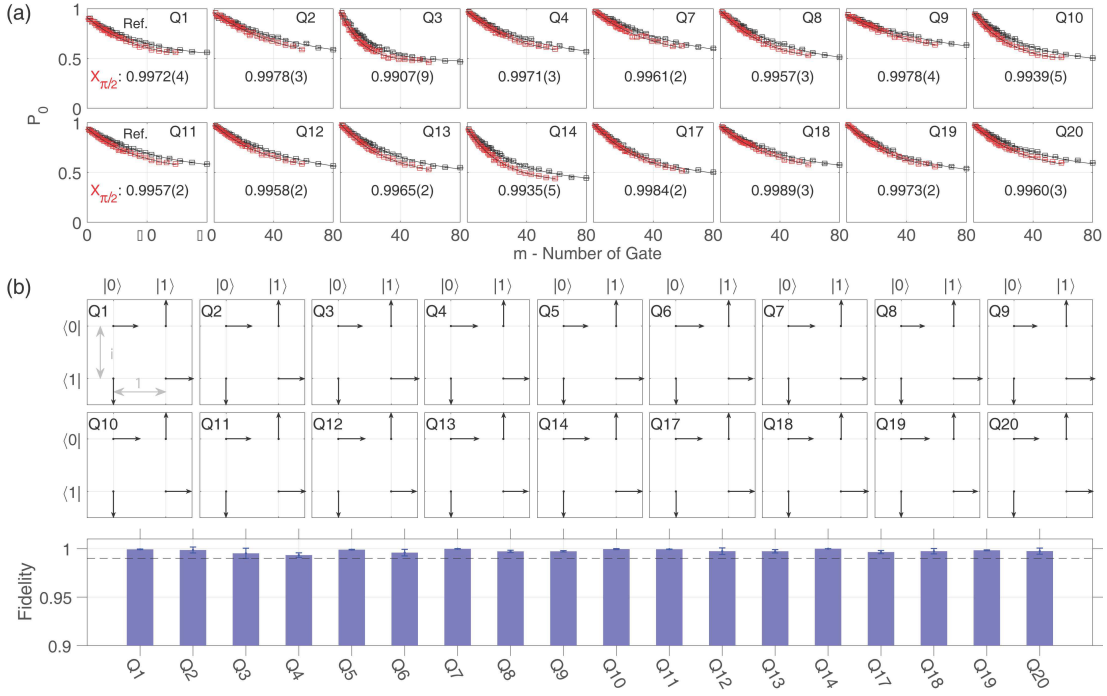


FIG. S2. **Calibrations of the single-qubit rotational gates for the GHZ experiment.** (a) 16-qubit simultaneous randomized benchmarking (RB) results with the single-qubit $X_{\pi/2}$ gate fidelities as listed. Each pulse sequence of the reference has up to m single-qubit Cliffords for each qubit [14]. Each Clifford includes additional idling gates to ensure that the j -th Cliffords on all 16 qubits can be synchronized. A final Clifford gate returns each qubit to $|0\rangle$. At the end of the pulse sequence we measure all 16 qubits simultaneously for 2^{16} occupation probabilities, based on which we perform partial trace over other qubits' indices for one piece of data on the target qubit; we sum over all data of $k = 30$ random pulse sequences for an exponential fit as shown in each panel. On average, each single-qubit Clifford consists of 0.375 gates from X_{π} , Y_{π} and I , 1.5 gates from $\pm X_{\pi/2}$ and $\pm Y_{\pi/2}$, and approximately 1.286 idling gates for synchronization. The pulse lengths of the X_{π} and Y_{π} gates are 80 ns, and the pulse lengths of all other gates are 40 ns. Black dots are the $|0\rangle$ -state probability data, P_0 , of each qubit as function of m for the reference, and red dots are data with $X_{\pi/2}$ inserted. (b) Single-qubit quantum state tomography characterizing the state $(|0\rangle - i|1\rangle)^{\otimes 18}$ prepared by applying $\pi/2$ gates on the 18 qubits, with the state preparation pulse sequence listed in zone I of Fig. 2(a) in the main text. 18 single-qubit density matrices are shown in the upper row, where the amplitude and phase of a matrix element are represented by the length and direction, respectively, of an arrow in the complex plane. The state fidelity metrics, shown in the bottom row, are all above 0.990 which agree with the RB results in (a).

are tuned to the interacting frequency, ω_I , for entanglement and then back to idle frequencies for further operations with rectangular pulses (see Fig. S3(a)), dynamic phases are accumulated which rotate the x - y axes in the Bloch sphere for each qubit by an angle proportional to the interacting time t . Precise calibration of these dynamic phases are needed for the following single-qubit rotational operations to ensure the reliability of the Q -function measurement.

Figure S3 shows how we track the dynamic phases in this process. We use a Ramsey interference measurement with the representative pulse sequence shown in Fig. S3(a) to calibrate one qubit at a time. Following the first $\pi/2$ rotation pulse, $X_{\pi/2}$, and after the target qubit Q_j returns to its idle frequency, a second $\pi/2$ pulse whose rotation axis is of phase ϕ in the x - y plane, $\phi_{\pi/2}$, is applied before the qubit is read out. To minimize the Q_j 's frequency shift due to all other qubits' existence through the ZZ -type crosstalk, we distribute the other

qubits in the vicinity of the interacting frequency ω_I , which is about 30 to 70 MHz away from $\omega_I/2\pi$, so that their combined effect on Q_j is the same as that when all qubits are biased to ω_I as calculated by the measured Z-crosstalk matrix \tilde{M}_Z (Fig. S1). The representative $|1\rangle$ -state probability, P_1 , data as functions of both the interacting time t and the phase difference $\phi - \delta \cdot t$, where $\delta = \omega_j - \omega_I$ is the qubit frequency detuning, are plotted in Fig. S3(b). By tracing the P_1 maximum values along the sliced data at each t value, shown as black dots in Fig. S3(b), we can estimate the extra rotated angle of the x - y axes that may be due to the imperfect experimental rectangular pulse. With the new orientation of the x - y axes in the Bloch sphere for this qubit being roughly located, we then perform an optimization search to fine tune the extra rotated angles of all qubits to maximize the fidelity of the experimentally detected state.

	$\omega_j^0/2\pi$ (GHz)	$\omega_j/2\pi$ (GHz)	$T_{1,j}$ (μ s)	$T_{2,j}^*$ (μ s)	$\lambda_{j,j+1}^c/2\pi$ (MHz)	$g_j/2\pi$ (MHz)	$\omega_j^r/2\pi$ (GHz)	$\omega_j^m/2\pi$ (GHz)	$F_{0,j}$	$F_{1,j}$
Q_1	5.698	4.320	~ 23	2.0	0.75	27.6	6.768	4.510	0.929	0.887
Q_2	5.611	4.791	~ 27	2.4	0.83	27.4	6.741	4.794	0.969	0.925
Q_3	5.793	5.330	~ 26	2.0	1.01	29.1	6.707	5.295	0.973	0.920
Q_4	5.729	4.865	~ 35	1.8	1.02	27.6	6.676	4.491	0.941	0.922
Q_5	5.585	4.490	~ 30	2.5	-0.39	26.5	6.649	4.435	0.946	0.911
Q_6	5.450	4.350	~ 29	3.0	1.07	29.2	6.611	4.310 (4.300)	0.927	0.893
Q_7	5.480	4.830	~ 36	2.7	1.10	27.8	6.589	4.399	0.967	0.885
Q_8	5.560	4.965	~ 37	2.5	0.83	30.1	6.558	4.905	0.954	0.919
Q_9	5.583	4.290	~ 20	2.9	0.79	24.1	6.551	4.370	0.933	0.896
Q_{10}	5.583	5.290	~ 33	2.7	0.65	27.7	6.513	5.375 (5.345)	0.977 (0.967)	0.846 (0.908)
Q_{11}	5.682	4.425	~ 35	2.8	0.77	27.3	6.524	4.290 (4.340)	0.943	0.889
Q_{12}	5.690	5.250	~ 33	1.8	0.81	26.9	6.550	5.345 (5.375)	0.981 (0.977)	0.876 (0.903)
Q_{13}	5.660	4.899	~ 31	2.0	0.96	29.1	6.568	4.819	0.986	0.934
Q_{14}	5.723	5.220	~ 51	2.4	1.08	27.4	6.598	4.885	0.993	0.951
Q_{15}	~ 5.7	4.290	~ 24	2.1	-0.21	26.3	6.640	4.34	0.981	0.903
Q_{16}	5.642	4.260	~ 37	2.8	0.77	26.5	6.659	4.01	0.966	0.925
Q_{17}	5.843	4.700	~ 51	2.3	0.91	27.3	6.685	4.850	0.989	0.940
Q_{18}	5.775	4.385	~ 37	1.2	0.54	29.0	6.712	4.465	0.967	0.924
Q_{19}	5.793	5.170	~ 46	2.0	0.67	24.6	6.788	4.930	0.950 (0.988)	0.875 (0.914)
Q_{20}	5.847	4.766	~ 37	1.7	0.64	27.5	6.758	5.839	0.991	0.813

TABLE S1. **Detailed device parameters and qubit performance metrics.** ω_j^0 is Q_j 's maximum resonant frequency at the sweet point, and ω_j is Q_j 's idle frequency where Q_j is initialized and single-qubit rotational pulses are applied. $T_{1,j}$ and $T_{2,j}^*$ are the typical single-qubit energy relaxation time and Ramsey dephasing time (Gaussian decay) [14], respectively, which are estimated based on the data measured around the interaction frequency where multiqubit GHZ states are generated. Note that $T_{1,j}$ may fluctuate over time due to the presence of two-level state defects [S1] and $T_{2,j}^*$ may not be relevant to the experiment since the qubits coupled with each other at the interacting frequency act as a coherent system which may become insensitive to the local flux noise within individual qubits [28]. $\lambda_{j,j+1}^c$ describes the crosstalk coupling strength between neighboring qubits, where j runs cyclically from 1 to 20. g_j is the coupling strength between Q_j and the bus resonator B . ω_j^r is the resonant frequency of the readout resonator for Q_j . ω_j^m is the resonant frequency of Q_j at the beginning of the qubit readout when Q_j 's readout resonator is unpopulated. Those values of ω_j^m for Q_6 , Q_{10} , Q_{11} , and Q_{12} in parentheses are used for the N -qubit GHZ experiment with N up to 18, during which Q_{15} and Q_{16} are biased to ~ 4 GHz and can be ignored. $F_{0,j}$ ($F_{1,j}$) is the typical probability of detecting Q_j in $|0\rangle$ ($|1\rangle$) when it is prepared in $|0\rangle$ ($|1\rangle$), which is used to correct raw probability data for elimination of the measurement errors [27]. Values in parentheses are for the GHZ experiment: As we switched from the 18-qubit GHZ experiment to the 20-qubit atomic Schrödinger cat state experiment, Q_{15} and Q_{16} were included so that we reconfigured the ω_j^m values of 4 qubits, and noticeable drops of a few percent in F_1 for Q_{10} , Q_{12} , and Q_{19} were captured since we adjusted the working parameters of Josephson parametric amplifiers.

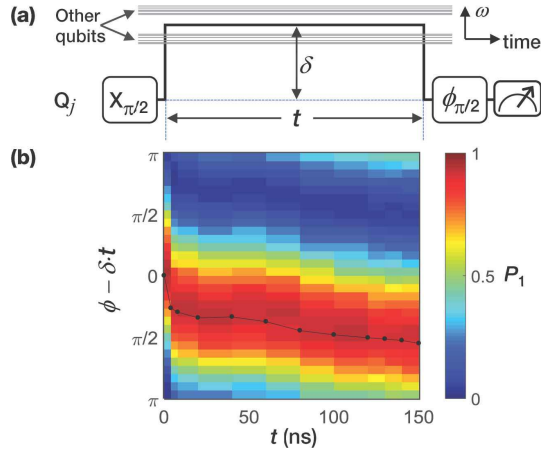


FIG. S3. **Phase tracking measurement.** (a) Pulse sequence of the Ramsey interference measurement used to determine the orientation of the x - y axes in the Bloch sphere for Q_j . (b) Representative experimental data with the pulse sequence shown in (a).

* C. S., K. X., and H.K. L. contributed equally to this work.

† hfan@iphy.ac.cn

‡ dzheng@iphy.ac.cn

§ hhwang@zju.edu.cn

[S1] P. V. Klimov *et al.*, Phys. Rev. Lett. **121**, 090502 (2018).